JOURNAL OF MAGNETIC RESONANCE IMAGING 36:1362–1371 (2012)

**Original Research**

# Accelerating Three-Dimensional Molecular Cardiovascular MR Imaging Using Compressed Sensing

Claudia Prieto, PhD,[1,2]* Marcelo E. Andia, MD,[1] Christian von Bary, MD,[3] David C. Onthank, PhD,[4] Tobias Schaeffter, PhD,[1] and Rene M. Botnar, PhD[1]

**Purpose:** To accelerate the acquisition of three-dimensional (3D) high-resolution cardiovascular molecular MRI by using Compressed Sensing (CS) reconstruction.

**Materials and Methods:** Molecular MRI is an emerging technique for the early assessment of cardiovascular disease. This technique provides excellent soft tissue differentiation at a molecular and cellular level using target-specific contrast agents (CAs). However, long scan times are required for 3D molecular MRI. Parallel imaging can be used to speed-up these acquisitions, but hardware considerations limit the maximum acceleration factor. This limitation is important in small-animal studies, where single-coils are commonly used. Here we exploit the sparse nature of molecular MR images, which are characterized by localized and high-contrast biological target-enhancement, to accelerate data acquisition. CS was applied to detect: (a) venous thromboembolism and (b) coronary injury and aortic vessel wall in single- and multiple-coils acquisitions, respectively.

**Results:** Retrospective undersampling showed good overall image quality with accelerations up to four for thrombus and aortic images, and up to three for coronary artery images. For higher acceleration factors, features with high CA uptake were still well recovered while low affinity targets were less preserved with increased CS undersampling artifacts. Prospective undersampling was performed in an aortic image with acceleration of two, showing good contrast and well-defined tissue boundaries in the contrast-enhanced regions.

**Conclusion:** We demonstrate the successful application of CS to preclinical molecular MR with target specific gadolinium-based CAs using retrospective (accelerations up to four) and prospective (acceleration of two) undersampling.

**Key Words:** cardiovascular; molecular imaging; MRI; compressed sensing; undersampling
**J. Magn. Reson. Imaging 2012;36:1362–1371.**


CARDIOVASCULAR MOLECULAR MRI is an emerging imaging technique for visualization and quantification of molecular differences among tissues by using target specific MR contrast agents (CAs) (1–3). This approach allows imaging of biological targets, by regionally modifying relaxation rates of the surrounding water protons. One promising application of molecular MRI is the earlier and more accurate assessment of cardiovascular risk, patient specific guidance of therapy and earlier assessment of therapy response. Novel cardiovascular imaging applications include atherosclerotic plaque characterization by identification of biological processes such as inflammation, extracellular matrix remodeling, angiogenesis, hypoxia, or thrombosis, which have been linked to an increased risk of plaque rupture (4–7). Other applications aim at the identification of risk of developing arrhythmias and left ventricular remodeling associated with progressive heart failure (e.g., detection of myocardial apoptosis, injury to extracellular matrix, and innervation) (8,9). The feasibility of in vivo molecular MR imaging has been demonstrated in several preclinical studies (small and large animal models) over the last decade and more recently in humans (10,11), showing the potential of this technique to be translated into the clinic in the near future.

In comparison with other medical imaging techniques such as single photon emission computed tomography (SPECT) and positron emission tomography (PET), molecular MRI has the advantage to provide both morphological as well as biological information with high spatial resolution. High spatial resolution is essential, for example, to visualize plaque area and positive remodeling or to measure thrombus diameter

[1]King's College London, Division of Imaging Sciences, and Biomedical Engineering, London, United Kingdom.
[2]Pontificia Universidad Catolica de Chile, Escuela de Ingenieria, Santiago, Chile.
[3]Klinik für Innere Medizin II, Universitätsklinikum, Regensburg, Germany.
[4]Lantheus Medical Imaging, North Billerica, Massachusetts, USA.
Contract grant sponsors: Lantheus Medical Imaging; National Institute for Health Research (NIHR).
*Address reprint requests to: Claudia P., Division of Imaging Sciences and Biomedical Engineering, 4th Floor, Lambeth Wing, St Thomas' Hospital, London, SE1 7EH, United Kingdom.
E-mail: claudia.prieto@kcl.ac.uk
Received March 31, 2011; Accepted June 21, 2012.
DOI 10.1002/jmri.23763
View this article online at wileyonlinelibrary.com.

and size. However the higher spatial resolution comes at the expense of increased acquisition times. These long scan times may limit the throughput of animal studies, prolong animal sedation times and increase the associated scanner costs.

Three-dimensional (3D) molecular MRI may be accelerated by the use of efficient imaging sequences and trajectories that provide faster coverage of *k*-space (12,13), by using parallel imaging techniques that take advantage of the spatial sensitivity of multiple receiver coils for complementary encoding (14–16), or by the use of novel reconstruction algorithms which recover the nonacquired data based on prior information or assumptions (17,18). Many of the theoretically efficient trajectories are prone to severe blurring and off-resonance artifacts. In parallel imaging the acceleration is limited by noise amplification due to the geometry factor of the receiver coils; this limitation is especially important in small animal studies where the availability of multiple channel coils is restricted. A recently introduced reconstruction algorithm is the Compressed Sensing (CS) (19–21) technique, which relies on the fact that sparse (or compressible) images can be recovered from randomly undersampled data by means of a nonlinear reconstruction.

Here, we propose to accelerate 3D high-resolution cardiovascular molecular MR imaging by the use of CS reconstruction. This approach exploits the inherent compressibility of most 3D molecular MRI applications, especially those using gadolinium based CAs, which are characterized by very localized and high T1-contrast enhancement. Gadolinium-based CA images are, in general, quasi-sparse in the image domain itself or in its finite-difference transform; whereas iron oxide images can be sparse in other domains such as discrete cosine transform (DCT), wavelet transforms or in positive contrast images (22–24). CS is an attractive reconstruction method for sparse 3D T1-weighted molecular MRI because of the described properties, because of the need for accelerated data acquisition and because it is not hardware dependent (it does not depend on number and/or configuration of coils). Moreover, the high signal to noise ratio (SNR) and contrast to noise ratio (CNR) usually achieved in the high-affinity targeted areas benefits the performance of CS reconstruction.

The aim of this study is to investigate the application of CS to gadolinium-based molecular MR images for single and multiple coil acquisitions. We consider two preclinical studies: (a) detection of venous thromboembolism in a mouse model of deep venous thrombosis (DVT) using a fibrin-binding contrast agent (25), and (b) detection of coronary artery remodeling and aortic vessel wall visualization using an elastin-binding contrast agent in a swine model of coronary stenting (26). Our interest in these studies was faster and accurate visualization of the presence or absence of contrast agent uptake to assess vessel wall thickness and thrombus size as an indicator of abnormality. Retrospective undersampling performance is analyzed for the mouse model (single coil acquisition). For the swine model (multiple coil acquisition) CS reconstruction is compared against SENSE and the effect of the CS reconstructions on quality measurements such as wall thickness and wall sharpness is also studied. CS acquisition with an acceleration factor of 2 (prospective undersampling) was also performed in the swine model.

## MATERIALS AND METHODS

### *Compressed Sensing Theory*

Compressed sensing theory states that sparse or compressible images can be recovered almost perfectly from randomly undersampled data by means of a nonlinear reconstruction. As pointed out in Lustig et al (21), CS reconstruction needs to satisfy three basic requirements: (a) The signal must be sparse after a known sparsifying transform (i.e., compressible), (b) the sampling must be incoherent with the sparsifying transform, and (c) a nonlinear reconstruction must be performed to recover the nonacquired data. The number of samples required to obtain an exact reconstruction represents an additional requirement. CS with $l_1$ norm minimization (as has been the usual case in MRI applications) achieves exact reconstruction when the number of acquired samples exceeds two to five times the sparsity of the image or its compressible version (27). Finally, in practice, a reliable recovery of the undersampled image depends also on the noise level, which should not dominate the signal in the image or its corresponding sparse transform domain, as it will be shown in the Results section.

Compressed sensing MRI reconstruction is achieved, in general, by solving the following quadratic constraint $l_1$ minimization problem (21):

$$Min\|\Psi\mathbf{m}\|_1 \quad \text{s.t.} \quad \|\mathbf{F_u m} - \mathbf{B}\|_2^2 < \varepsilon, \qquad [1]$$

where $\|\mathbf{x}\|_1 = \sum_i |x_i|$ and $\|\mathbf{x}\|_2^2 = \sum_i x_i^2$ denotes the $l_1$ norm and $l_2$ norm of a vector $\mathbf{x}$, $\mathbf{m}$ is the vectorized reconstructed image, $\Psi$ is the sparsifying transform (e.g., DCT, wavelets, finite differences, etc.), $\mathbf{F}_u$ is the undersampled Fourier encoding matrix, $\mathbf{B}$ is the measured *k*-space data and $\varepsilon$ is an estimated upper bound on the power of the additive white Gaussian noise $\mathbf{n}$ in $\mathbf{B}$, i.e.,:

$$\mathbf{B} = \mathbf{F_u m} + \mathbf{n}, \ \text{with} \ \|\mathbf{n}\|_2 < \varepsilon. \qquad [2]$$

The cost function $\|\Psi\mathbf{m}\|_1$ in Eq. [1] enforces sparsity by minimizing the sum of absolute values of the elements in the sparse domain; whereas the constraint term $\|\mathbf{F_u m} - \mathbf{B}\|_2 < \varepsilon$ ensures the consistency between the reconstructed and the acquired data considering noisy measurements.

Sparsity in the image domain was exploited for all investigated applications. In this case, sparsity means that only relatively few pixels of the image exhibit high intensity values whereas most of the remaining pixels have low enough intensity values that can be neglected. In average, 6% to 12% of the pixels present relevant intensities in the applications investigated in this study, considering as relevant those intensities

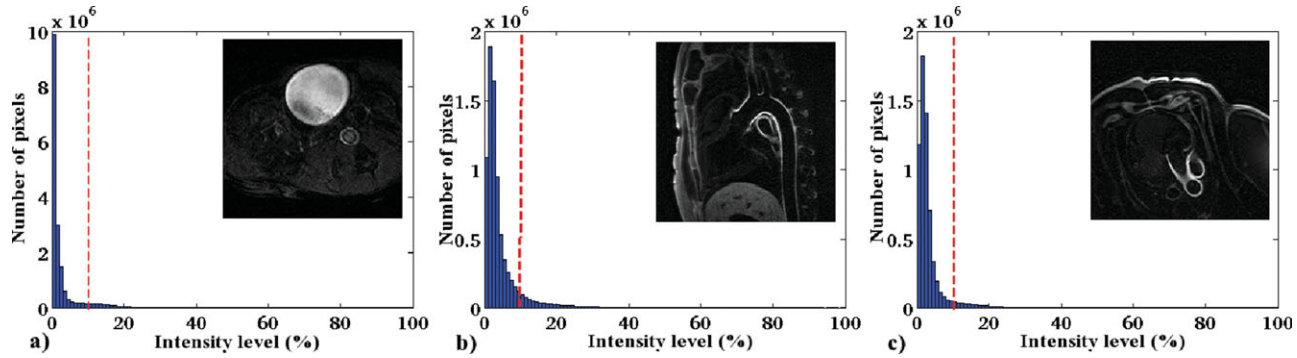


**Figure 1.** Sparsity in the image domain for 3D gadolinium-based molecular imaging. In this case, sparsity means that there are relatively few pixels of the image with high intensity values, whereas the remaining pixels have low enough intensity values that can be neglected. The image histogram is included for (**a**) thrombus, (**b**) aortic wall, and (**c**) LAD coronary images. In all cases, only a few number of pixels of the image exhibit intensities values higher than 10% of the maximum signal.

higher than 10% of the maximum signal. This is shown in Figure 1 for thrombus, aortic wall and coronary images. In gadolinium-based molecular MR images the high intensities values correspond, mainly, to very localize high T1-contrast enhancement.

### *Acquisition Scheme and Image Reconstruction*

Inversion recovery (IR) fat suppressed acquisitions were performed in both preclinical studies to promote image sparsity by blood and fat signal nulling. For the retrospective undersampling, a random pattern was implemented (Cartesian trajectory) by minimizing the sidelobe-to-peak ratio of the point spread function (PSF) (21). A random undersampling pattern (with no optimization of the sidelobe-to-peak ratio) was implemented on the scanner and used for the prospective CS acquisition. The center of the *k*-space (10% in each direction) was fully sampled in both cases. An example of sampling pattern is shown in Figure 2 for a matrix size of 128 × 128 and undersampling factor of four. *K*-space was sampled in a linear manner to minimize eddy current artifacts.

CS reconstructions were performed solving the constraint optimization problem in Eq. [1] using a recently introduced first-order method for sparse recovery referred as Nesterov's algorithm (28). This is an iterative algorithm where each iteration is decomposed into three steps, each involving only a few matrix-vector operations. This is an extension of Nesterov's smoothing technique, which minimizes nonsmooth convex functions substituting them by a smooth approximation. This algorithm is characterized by an accelerated convergence rate, and does not depend on the tuning of several parameters or specific tunings for different data sets. Moreover, the accuracy of this approach is especially suitable for the reconstruction of compressible (rather than sparse) images and for images that exhibit a high intensity range, as is the case in molecular MR imaging.

Image reconstruction was performed with Matlab (The Mathworks, Natick, MA) on a Dual 4-Core PC with 32GB memory. The reconstructions were performed directly in the 3D data sets to exploit 3D sparsity, rather than solving a series of 2D reconstructions considering each slice in the readout direction independently. The reconstruction time per volume was in average 5 min per data set, allowing a maximum of 100 iterations. The only parameter modified for the different reconstructions was the value of the upper bound for the noise level (ε), which was chosen based on the power noise estimated from the high frequencies of the acquired *k*-space data.

### *In Vivo Experiments*

All studies were performed under the approval of the hospitals Animal Care and Use Committee on Animal Investigations.

#### *Venous Thromboembolism Model*

A fibrin specific MR contrast agent (EP-2104R, EPIX Pharmaceuticals, MA) was used in an animal model study of venous thrombosis (25). Adequate thrombus visualization and accurate thrombus size estimation are required from MR imaging.

*Imaging Protocols.* MRI acquisition was performed on a 3T scanner (Philips Achieva, Best, The Netherlands) using a dedicated small animal surface coil (single channel loop coil, diameter = 47 mm). Images were acquired at day 7 following thrombus induction and 3 hours after administration of 8 μmol/kg of the fibrin-binding contrast agent (4,29). Cardiac gating was used and animals were scanned under anesthetic sedation. To determine the optimal inversion time (TI) for blood signal nulling, a Look-Locker sequence was performed. This was followed by an IR 3D fast gradient echo (TFE) sequence for selective visualization of the thrombus and cava vein vessel wall. Relevant scan parameters included: field-of-view (FOV) = 45 × 45 × 15 $mm^3$, resolution = 0.1 × 0.1 × 1 $mm^3$ reconstructed to 50 × 50 × 500 $\mu m^3$, repetition time (TR) = 42 ms, echo time (TE) = 13 ms, flip angle = 30°, averages = 2, total acquisition time ~ 20 min.

*Image Reconstruction.* The fully sampled acquired data was retrospectively undersampled with factors from 2 to 7, relative to the reconstructed matrix size.

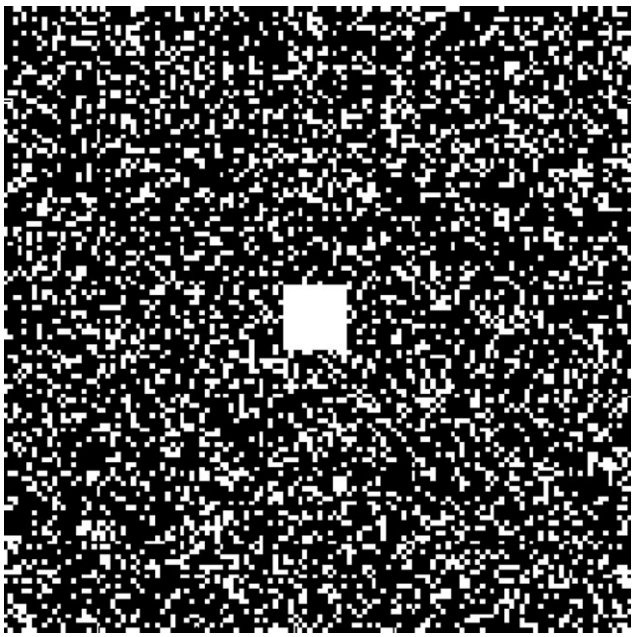

**Figure 2.** Example of random pattern for a matrix size of 128 × 128 and undersampling factor of 4.

Root mean square (RMS) error and thrombus wall depiction were compared against the fully sampled acquisition in each case.

*Image Analysis.* Thrombus diameter was calculated for the undersampled acquisitions, and compared with the measurements from the fully sampled image.

### *Coronary and Aortic Vessel Wall Model*

Contrast enhancement on coronary vessel wall stent and aortic wall were achieved using an elastin-binding (BMS753951, Lantheus Medical Imaging, MA) MR agent (26). Adequate wall visualization and accurate wall sharpness and thickness estimation are required from MR imaging.

*Imaging Protocols.* MRI acquisition was performed on a 1.5T scanner (Philips Achieva, Best, The Netherlands) equipped with a five-channel cardiac receiver coil and swine were scanned in supine position. Images were acquired 4 weeks after stent placement and 1 h after administration of 0.1 mmol/kg of the elastin-binding contrast agent, injected intravenously by means of the left or right ear vein. After determining the optimal TI for blood signal nulling with a Look-Locker sequence, three T1-weighted 3D IR TFE sequences were performed in sagittal orientation to visualize: (a) the left anterior descending (LAD), (b) right coronary artery (RCA), and (c) aortic vessel wall. The free breathing imaging sequences were cardiac-triggered, navigator gated, and fat suppressed. Coronary artery imaging parameters included FOV = 320 × 320 × 45 $mm^3$, resolution = 1.25 × 1.25 × 3 $mm^3$ reconstructed to 0.625 × 0.625 × 1.5 $mm^3$, TR/TE/flip angle = 5.95/1.83 ms/30°, averages = 1. Aortic wall imaging parameters included: FOV = 320 × 320 × 45 $mm^3$, resolution = 1.25 × 1.25 × 3 $mm^3$ reconstructed to 0.625 × 0.625 × 1.5 $mm^3$, TR = 4.88 ms, TE = 1.55 ms, flip angle = 30°. Total imaging time was approximately 11 min per 3D dataset (with navigator efficiencies of 35% to 55%).

Fully sampled acquisitions were performed in seven swine and a CS undersampled acquisition with acceleration factor of 2 was performed to image the aortic wall in the eighth swine. All parameters, beside the acceleration factor, were kept as described above. Due to scan time constraints it was not possible to prospectively acquire in vivo data with different acceleration factors. A fully sampled acquisition was also performed in this case for comparison purposes.

*Image Reconstruction.* For image quality analysis the fully sampled data was retrospectively undersampled with factors from 2 to 7 for the aortic wall images and with undersampling factors up to 3 for the coronary acquisitions (relative to the reconstructed image matrix). Retrospective undersampling was performed after interpolation from the acquired (1.25 × 1.25 × 3 $mm^3$) to the reconstructed (0.625 × 0.625 × 1.5 $mm^3$) resolution and after sum of squares coil combination. RMS errors were compared against the fully sampled acquisition in each case. To compare with the SENSE algorithm, retrospective undersampling was performed in *k*-space at the acquired resolution (1.25 × 1.25 × 3 $mm^3$). CS reconstruction was performed coil by coil and single-coil images were combined using the sum of squares approach.

As the quality of CS reconstruction depends on the noise level of the acquisitions, the effect of SNR degradation on the quality of the reconstructions was studied in the LAD and aortic wall images of one swine. Gaussian noise was added to the fully sampled acquisitions to degrade the SNR of the LAD coronary artery image from 28 to 21.02, 17.02, 13.03, 10.04, 7.06 and 4.1; and of the aortic wall image from 105 to 100, 75, 38.01, 30.01, 17.02, 15.03 and 9.05. SNR was computed by taking the mean signal from a region of interest (coronary wall and aortic wall, respectively) and the standard deviation of the noise from a region in the background (air). Because magnitude images were used, the mean signal was corrected according to (30). This set of images was reconstructed with undersampling factors of up to 4 for coronary images, and up to 5 for aortic wall images. The experiment was repeated 4 times with different random undersampling patterns but using the same undersampling factors, and the average of the RMS errors was computed for each case. The RMS error was computed in a region of interest (ROI) around the LAD coronary artery and the aortic arch, respectively.

For comparison purposes, SENSE reconstruction was also performed in one aortic vessel wall image. Fully sampled images were retrospectively undersampled using a uniform Cartesian pattern with acceleration factors of up to 4. Undersampling of 2 and 3 were performed in the anterior–posterior (AP) direction, while the undersampling of 4 was achieved using an undersampling factor of 2 in the AP and

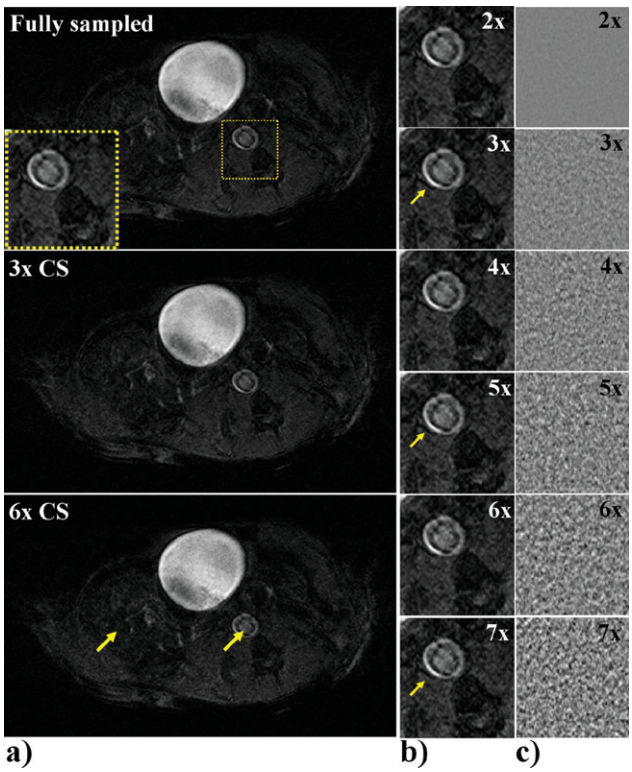


**Figure 3.** Compressed sensing (CS) reconstruction results for venous thromboembolism images (mouse model) with retrospective undersamplings of 2 to 7. (**a**) Reconstructed images for undersampling factors (R) of 3 and 6 in comparison with the fully sampled acquisition, (**b**) ROI (indicated in Fig. 3a) for images reconstructed with R = 2 to 7. (**c**) Windowed difference between fully sampled and reconstructed images for the specified ROI with undersamplings of 2 to 7. Good overall image quality is observed for R up to 4. Increased CS undersampling artifacts in low intensities tissues is noticeable with R = 5 to 7, however good depiction of the contrast-enhanced areas is still observed (arrows in Fig. 1a,b). [Color figure can be viewed in the online issue, which is available at wileyonlinelibrary.com.]

right–left (RL) direction, respectively. The coil sensitivity maps for the SENSE reconstruction were estimated from the center of the *k*-space. Due to the required orientation (sagittal) just two coils in the phase-encoding (AP) direction and ~1 coil in the slice (RL) direction were available to solve the undersampling problem. Therefore acceleration factors higher than 2 are challenging with SENSE reconstruction, but were included here for comparison purposes.

*Data analysis.* The effect of undersampling on vessel wall sharpness and thickness were analyzed for the aortic wall images (N = 7). Vessel wall sharpness (31) and thickness were estimated using the Soap-Bubble tool (32), as commonly used for coronary images. Vessel wall sharpness is defined as the average edge value along the vessel border; therefore a vessel sharpness of 100% refers to a maximum signal intensity change at the vessel edge with the mean signal along the centerline of the vessel wall being used to normalize the vessel wall sharpness. Measurements were performed independently by two reviewers blinded to the undersampling factor of the reconstructed images. Reported results correspond to the average from the two reviewers. Measurements from the undersampled reconstructions and the fully sampled image were compared using an unpaired Student's t-test. Statistical significance was defined as $P < 0.05$.

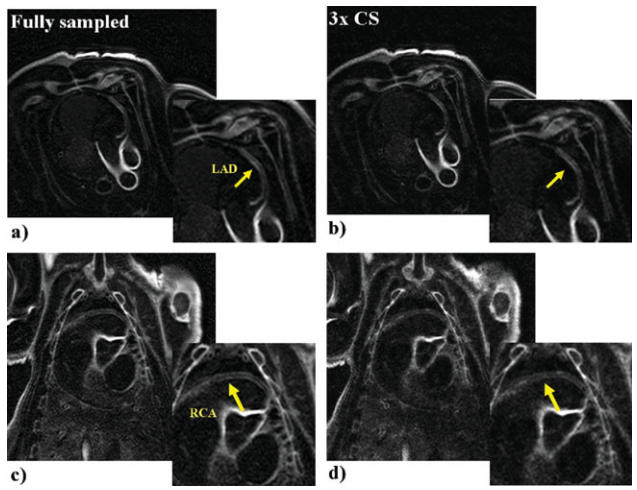


**Figure 4.** CS reconstruction results for LAD (injured) and RCA (noninjured) coronary artery (swine model) with a retrospective undersampling of 3. Reformatted images along the coronary artery plane are shown: (**a,c**) Fully sampled image; (**b,d**) 3x CS reconstructed image. Enlarged view of a ROI for the fully sampled and the reconstructed images are also included. Good depiction of the contrast-enhanced coronary wall is observed for the LAD CS reconstruction; however, blurring can be observed in the RCA due to lower contrast agent uptake (arrows). [Color figure can be viewed in the online issue, which is available at wileyonlinelibrary.com.]

## RESULTS

### *Venous Thromboembolism Model*

Reconstruction results for undersampling factors of 3 and 6 in comparison with the fully sampled image are shown in Figure 3a for a selected slice (middle segment of the thrombus). Enlarged views of a ROI around the thrombus are included for undersampling

Table 1
Quality Measurements for a Venous Thromboembolism Reconstruction With Undersampling Factors of R = 2 to 7, in Comparison With the Fully Sample Image (R = 1)*

| | R = 1 | R = 2 | R = 3 | R = 4 | R = 5 | R = 6 | R = 7 |
|---|---|---|---|---|---|---|---|
| Diameter (mm) | 3.3 | 3.3 | 3.4 | 3.4 | 3.4 | 3.4 | 3.5 |
| RMS error (%) | – | 0.25 | 0.68 | 0.9 | 1.05 | 1.13 | 1.27 |

*Root mean square (RMS) error and thrombus diameter estimations are shown for each case.

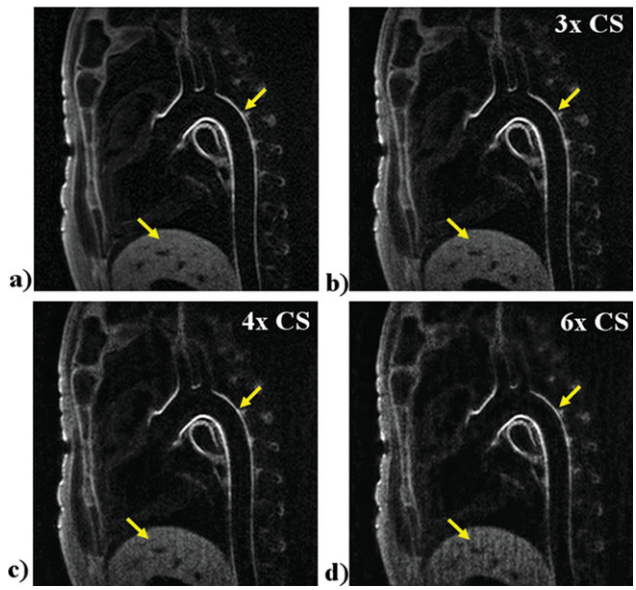


**Figure 5.** Reformatted aortic wall images (swine model) after CS reconstruction with retrospective undersampling factors of 3, 4, and 6: (**a**) Fully sampled image, (**b**) 3x CS reconstructed image, (**c**) 4x CS reconstructed image, (**d**) 6x CS reconstructed image. Contrast-enhanced areas (aortic vessel wall) demonstrate preservation of high signal intensities and image sharpness; whereas weak intensity regions, such as the liver, present reconstructions errors for high undersampling factors (arrows on the aortic wall and liver). [Color figure can be viewed in the online issue, which is available at wileyonlinelibrary.com.]

factors of 2 to 7 in Figure 3b. The difference images between the fully sampled and the undersampled reconstructions are also shown in Figure 3c for the specified ROI. RMS errors in comparison with the fully sampled image are reported in Table 1.

Thrombus diameter values for undersampling factors of up to 7 in comparison with the fully sampled acquisition are reported in Table 1. Small errors were observed for undersampling factors up to 4 (Table 1). CS undersampling artifacts errors and underestimation of high intensities values were observed for undersampling factors $> 5$ (Fig. 3c) but not affecting considerably thrombus diameter estimation (Table 1).

### *Coronary and Aortic Vessel Wall Model*

Reconstruction results for LAD (stent) and RCA (noninjured) coronary arteries with an undersampling factor of 3 are shown in Figure 4. Reconstructed images were reformatted along the coronary artery plane using the Soap-Bubble tool. The fully sampled and CS reconstructed images are shown in Figure 4a,b (LAD) and Figure 4c,d (RCA). Two ROIs including the coronary artery are also shown for the fully sampled and CS reconstructions. Good depiction of the LAD coronary wall was achieved with the CS reconstruction (Fig. 4b). Poorer coronary wall depiction was observed for the noninjured RCA vessel wall due to less contrast agent uptake and lower SNR (Fig. 4d). The SNR was 28 for the fully sampled LAD coronary image and only 17 for the fully sampled RCA acquisition.

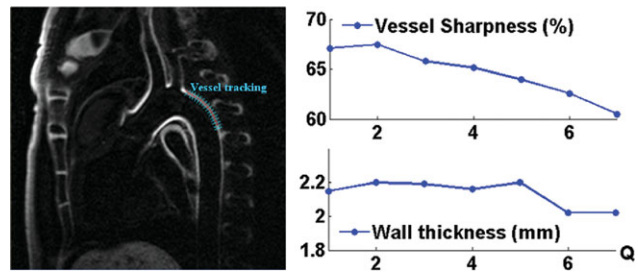


**Figure 6.** Quality measurements for an aortic wall reconstruction with undersampling factors of R = 2 to 7, in comparison with the fully sampled image (R = 1). Vessel wall sharpness and thickness were estimated in the indicated region of the aortic arch wall. [Color figure can be viewed in the online issue, which is available at wileyonlinelibrary.com.]

CS reconstruction results for aortic wall images with undersampling factors of 3, 4 and 6 in comparison with the fully sampled image are shown in Figure 5. Reconstructed images were reformatted along the course of the descending aorta using the Soap-Bubble tool. Reconstructions with undersampling factors of 3 and 4 were in good agreement with the fully sampled image with RMS errors of 0.79% and 0.88% respectively, whereas the RMS error increased to 1.23% for an undersampling of 6.

Quality measurements for the aortic wall reconstructions with undersampling factors of 2 to 7 are shown in Figure 6 for a specific data set. High levels of vessel sharpness (>60%) were achieved for all acceleration factors while aortic vessel wall thickness was preserved for undersampling factors up to 5. Analysis of quality measurements for all reconstructed aortic wall data sets (N = 7) is shown in Table 2 including aortic vessel wall thickness and sharpness, as well as RMS error. Good reconstruction quality was observed for all measurements with undersampling factors $\leq 4$.

Table 2
Quality Measurements Analysis for Aortic Wall Reconstructions (N = 7) With Undersampling Factors of R = 2 to 7, in Comparison With the Fully Sample Image*

| Mean ± SD of difference | R = 2 | R = 3 | R = 4 | R = 5 | R = 6 | R = 7 |
|---|---|---|---|---|---|---|
| Wall thickness error (%) | 0.28 ± 0.20 | 0.71 ± 0.80 | 2.38 ± 1.97 | 4.69 ± 2.59 | 4.46 ± 3.88 | 5.44 ± 3.99 |
| Wall sharpness loss (%) | −0.25 ± 0.3 | 0.87 ± 0.61 | 0.76 ± 1.72 | 1.80 ± 3.65 | 2.59 ± 3.99 | 1.74 ± 3.01 |
| RMS error (%) | 0.60 ± 0.08 | 1.04 ± 0.21 | 1.30 ± 0.35 | 1.79 ± 0.56 | 1.79 ± 0.56 | 1.98 ± 0.62 |

*Percentage difference between the values obtained for the undersampling reconstructions and the ones obtained for the fully sampled image are reported for wall thickness and wall sharpness. Root mean square (RMS) errors for the different reconstructions respect to the fully sampled image are also included. Mean ± Standard deviation is reported. Measurements from the undersampled reconstructions and the fully sampled image were compared using an unpaired Student's t-test ($P = 0.05$). Nonsignificant difference was obtained in all cases.

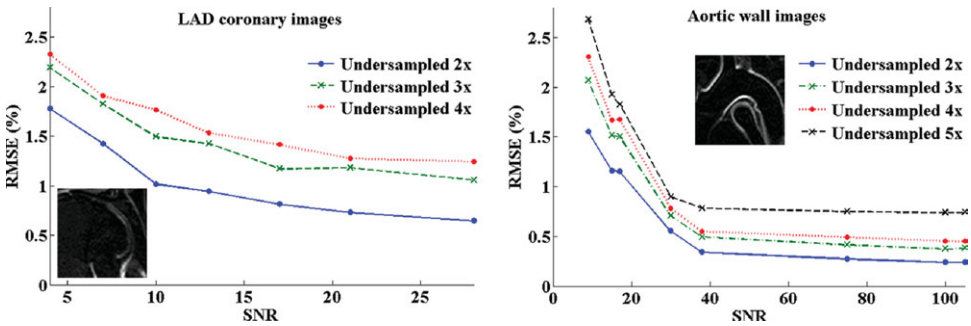


**Figure 7.** Effect of the SNR degradation in the quality of CS reconstructions for (left) LAD coronary and (right) aortic wall images. RMS errors were computed on the specified ROIs around the proximal LAD and the aortic wall, respectively. [Color figure can be viewed in the online issue, which is available at wileyonlinelibrary.com.]

The effect of SNR degradation on image quality is shown in Figure 7 for the LAD and aortic wall images. In all cases the RMS error increases while SNR decreases. For the LAD images, a gradual increase of the reconstruction error was observed for images with SNR values between 10 and 28 while a larger increase was observed for SNR values below 10. Similar findings were made for the aortic wall images (Fig. 7).

The comparison between CS and SENSE reconstructions is shown in Figure 8 for an aortic wall image. Reformatted undersampled reconstructions (R = 2 to 4) are shown for each method in comparison with the fully sampled image. For an undersampling factor of 2 both reconstructions, CS and SENSE, were in good agreement with the fully sampled acquisition with RMS errors of 1.97% and 2.19%, respectively. For an undersampling factor of 3, residual aliasing and increased noise was observed with SENSE reconstruction (arrow in Fig. 8c), conversely good reconstruction quality in the contrast-enhanced areas was obtained with the CS method. However, CS undersampling artifacts remained in the myocardium and liver for the 3x CS reconstruction (arrow in Fig. 8f). RMS errors with respect to the fully sampled image were of 2.24% and 2.68% for the CS and SENSE reconstructions, respectively. Remaining aliasing artifacts and increased noise was observed in SENSE reconstructions with an undersampling factor of 4 (Fig. 8d). With CS reconstruction, increased CS undersampling artifacts were observed in the myocardium and liver, and light blurring was found in the aortic wall for the same undersampling factor (Fig. 8g). RMS errors with respect to the fully sample image were of 2.37% and 4.00% for the CS and SENSE reconstructions, respectively.

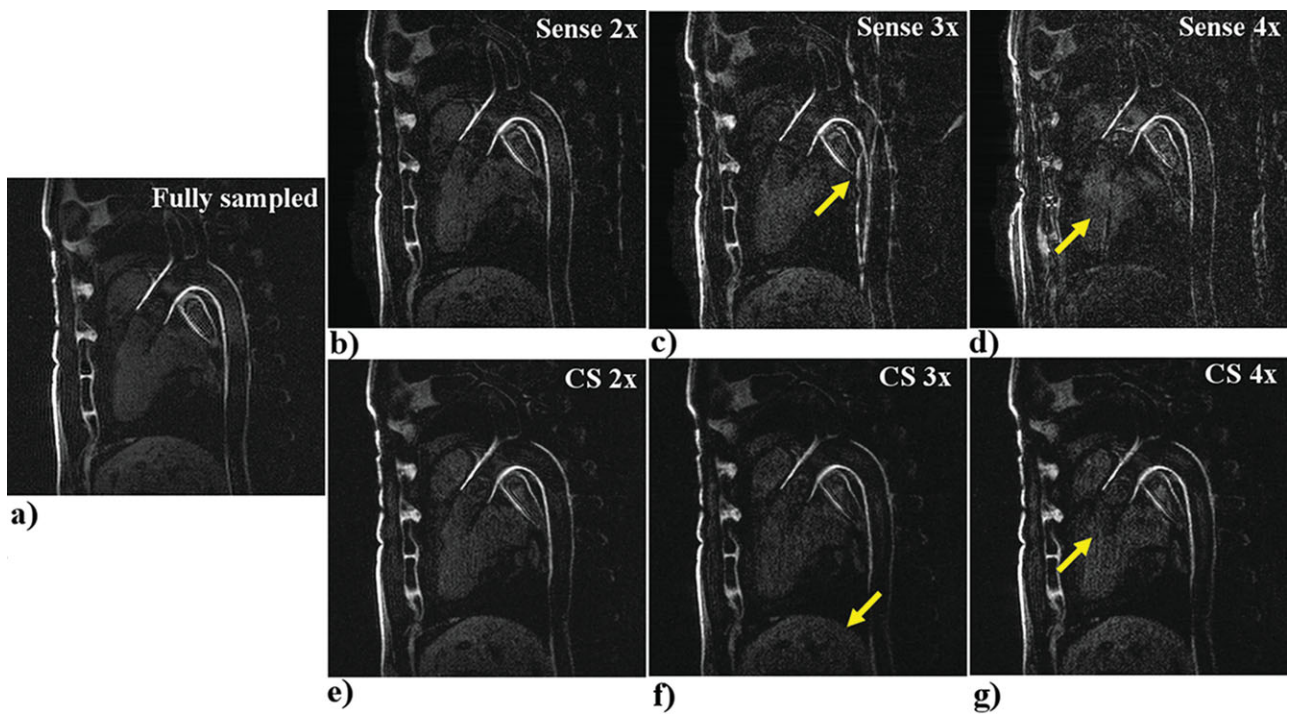


**Figure 8.** Comparison between CS and SENSE reconstructions for undersampling factors of 2 to 4 in reformatted aortic wall images (swine model). (**a**) Fully sampled image, (**b**) 2x SENSE reconstruction, (**c**) 3x SENSE reconstruction, (**d**) 4x SENSE reconstruction, (**e**) 2x CS reconstruction, (**f**) 3x CS reconstruction, (**g**) 4x CS reconstruction. Residual aliasing and increased noise is observed for SENSE reconstructions with undersampling factors of 3 and 4 (arrows). Good agreement with the fully sampled image is achieved with CS reconstruction for acceleration factors of 2 and 3, however CS undersampling artifacts in low intensity regions (i.e., myocardium and liver) and slight blurring in the aortic wall is observed for an undersampling factor of 4 (arrows). [Color figure can be viewed in the online issue, which is available at wileyonlinelibrary.com.]

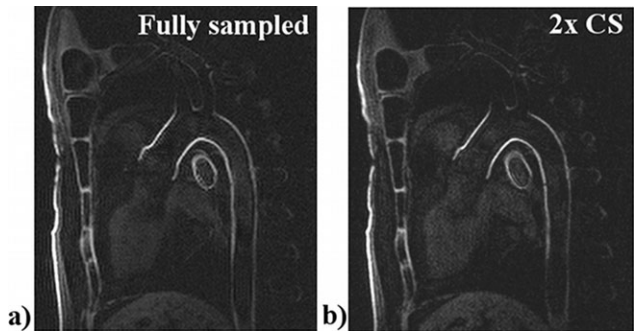


**Figure 9.** CS reconstruction for a CS acquisition (prospective undersampling) in aortic wall image (swine model): (a) Fully sampled image, (b) 2x CS reconstruction. Reconstructed image is in good agreement with the fully sampled acquisition, preserving contrast and resolution of the contrast-enhanced features (i.e., aortic vessel wall).

The reconstruction result for a CS acquisition (R = 2) of an aortic wall image is shown in Figure 9b. A fully sampled acquisition performed in the same swine is included in Figure 9a. Vessel wall thickness and sharpness were measured in the reformatted images as was described for the retrospective experiments. Despite the shorter acquisition time, and slight differences in heart rate and respiratory motion between both acquisitions, quantitative measurements showed good agreement. Vessel wall sharpness and thickness were 70.9% versus 67.8% and 1.93 mm versus. 1.82 mm for the fully sampled and undersampled acquisitions, respectively.

## DISCUSSION

High spatial resolution, adequate SNR, and short acquisition times are often requirements in molecular MRI. The use of specific CAs is aimed at creating regionally modified relaxation rates in the tissue of interest to provide both high SNR and CNR in the contrast enhanced areas, while providing low SNR and CNR in other image regions thereby creating sparse images (in this case, sparsity means that there are relatively few pixels of the image with high intensity values whereas the remaining pixels have low enough intensity values that can be neglected). This characteristic makes molecular MRI an ideal application for CS reconstruction. In this work we have demonstrated the successful application of CS to preclinical applications with target specific gadolinium based contrast agents. Retrospective undersampling with different acceleration factors allowed quantification of quality measures of CS reconstructions. Prospectively undersampled acquisition in a swine model provided initial evidence of the feasibility of using CS for molecular imaging of aortic vessel wall enhancement.

Sparsity was exploited in the image domain itself, without the use of total variation regularization, aimed at keeping the reconstruction process robust and efficient. Robustness was achieved by reducing the number of tuning parameters (e.g., regularization parameters) as well as by avoiding specific tuning for different data sets. Efficiency was achieved by using an algorithm suited for large-scale reconstructions and avoiding time consuming sparsifying transformations (direct and inverse). To increase sparsity in the image domain fat suppression was applied in all acquisitions. The only parameter that had to be modified for the different reconstructions was the value of $\epsilon$, which was chosen based on the power noise of the undersampled data. Reconstructions were performed directly in the 3D data sets to exploit 3D sparsity, taking approximately 5 min per data set.

Results for retrospectively undersampled experiments showed negligible errors with acceleration factors of up to 4 for the venous thrombus and aortic wall images, up to 3 for the LAD (injured) images, and up to 2 for RCA (noninjured, less contrast agent uptake) images. Contrast-enhanced areas demonstrated preservation of high signal intensities and image sharpness in all cases. For higher acceleration factors, CS undersampling artifacts were observed for some low intensity anatomic regions (such as the liver in the aortic wall images), while features with high contrast agent uptake were still well recovered. This is a characteristic of CS reconstruction and is suitable for molecular MR images, where the areas of interest exhibit high signal intensity. This property allowed recovering contrast-enhanced areas even for high acceleration factors. Assessment of the effect of CS reconstructions on image quality measures such as wall thickness and wall sharpness in aortic wall was performed for different undersampling factors. Good reconstruction quality was observed in all the measurements with undersampling factors up to 4. Vessel wall thickness and sharpness measurements were in good agreement with the values from the fully sampled images even for higher undersampling factors (percentage difference less than 6%).

As alluded above, in the studied applications the interest was in the visualization of presence or absence of contrast agent uptake as an indicator of abnormality (i.e. fibrin binding in intravascular thrombus and binding of elastin in coronary injuries and aortic wall). The high spatial resolution was required not just for visualization but also to quantify measures such as thrombus diameter and vessel wall thickness. There are several other applications in cardiovascular molecular MRI with similar objectives, such as presence of inflammation, quantification of ischemic areas and vascular remodeling. Another purpose of molecular MRI, not addressed in this study, is the quantification of SNR and CNR to assess, e.g., treatment response. Further research must be performed in this topic because noise estimation is difficult in CS reconstructions, due to the variable noise level across the FOV and its intrinsic denoising property. As in parallel imaging reconstruction approaches like estimating noise from additional noise scans or Monte Carlo simulations may be investigated.

Adequate SNR is needed for good performance of CS reconstruction. The effect of the SNR degradation in the quality of the reconstructions (quantified by the RMS error) was studied in LAD coronary and aortic wall images for different retrospective undersampling

factors. In all cases the RMS error increased while SNR decreased. Steeper rise of the RMS error was obtained when SNR dropped below 10 for the coronary images and below 27 for the aortic wall acquisitions. This suggests that lower undersampling factors should be used when the clinically relevant tissue correspond to a low affinity target, whereas higher undersampling factors could be used for high affinity targets.

Comparison between CS and SENSE reconstructions showed a better performance for the CS approach for high undersampling factors. A low performance of SENSE was expected for undersampling factors higher than 2 due to the reduced number of coil elements available to resolve the reconstruction (2 in the phase-encoding direction and ~1 in the slice direction). This is because SENSE does not exploit the high contrast and sparsity nature of the molecular MR images, but only the redundancy of the spatial encoded data. Nevertheless, CS can be combined with parallel imaging techniques to further speed up acquisitions as has been shown before (33,34).

A prospectively undersampled acquisition of the aortic wall with an undersampling factor of 2 showed negligible loss of contrast, tissue boundaries and resolution in the contrast-enhanced regions, despite the shorter acquisition time. Higher undersampling factors and optimized undersampling patterns, as well as the feasibility of increasing spatial resolution through scan time reduction, will be studied in future experiments for prospective undersampling.

In conclusion, accelerated 3D molecular MR imaging using CS has been demonstrated for preclinical applications with gadolinium based CAs. The compressibility requirement of CS is satisfied in most of these molecular MR images, due to the highly localized T1-contrast enhancement produced by the target-specific CAs. The high SNR and CNR in the targeted areas benefit the performance of CS reconstruction. Moreover, CS is especially useful for small animal studies where parallel imaging techniques often cannot be applied due to the limited availability of multi channel small animal coils. Good overall image quality was demonstrated with retrospective acceleration factors up to 4 in studies on mouse and swine models, and with an acceleration factor of 2 in a prospective acquisition on the swine model. For higher acceleration factors high contrast features were still well recovered, however low intensity regions were less preserved with increased CS undersampling artifacts.

## ACKNOWLEDGMENTS

Lantheus Medical Imaging provided the elastin binding contrast agent. Financial support was received from the Department of Health by means of the National Institute for Health Research (NIHR) comprehensive Biomedical Research Centre award to Guy's & St Thomas'.

## REFERENCES

1. Wu JC, Bengel FM, Gambhir SS. Cardiovascular molecular imaging. Radiology 2007;244:337–355.
2. Sosnovik DE, Nahrendorf M, Weissleder R. Molecular magnetic resonance imaging in cardiovascular medicine. Circulation 2007; 115:2076–2086.
3. Saraste A, Nekolla SG, Schwaiger M. Cardiovascular molecular imaging: an overview. Cardiovasc Res 2009;83:643–652.
4. Botnar RM, Buecker A, Wiethoff AJ, et al. In vivo magnetic resonance imaging of coronary thrombosis using a fibrin-binding molecular magnetic resonance contrast agent. Circulation 2004;110: 1463–1466.
5. Amirbekian V, Lipinski MJ, Briley-Saebo KC, et al. Detecting and assessing macrophages in vivo to evaluate atherosclerosis noninvasively using molecular MRI. Proc Natl Acad Sci U S A 2007; 104:961–966.
6. Meding J, Urich M, Licha K, et al. Magnetic resonance imaging of atherosclerosis by targeting extracellular matrix deposition with Gadofluorine M. Contrast Media Mol Imaging 2007;2: 120–129.
7. Korosoglou G, Weiss RG, Kedziorek DA, et al. Noninvasive detection of macrophage-rich atherosclerotic plaque in hyperlipidemic rabbits using "positive contrast" magnetic resonance imaging. J Am Coll Cardiol 2008;52:483–491.
8. Hiller KH, Waller C, Nahrendorf M, Bauer WR, Jakob PM. Assessment of cardiovascular apoptosis in the isolated rat heart by magnetic resonance molecular imaging. Mol Imaging 2006;5: 115–121.
9. Spuentrup E, Ruhl KM, Botnar RM, et al. Molecular magnetic resonance imaging of myocardial perfusion with EP-3600, a collagen-specific contrast agent: initial feasibility study in a swine model. Circulation 2009;119:1768–1775.
10. Makowski MR, Ebersberger U, Nekolla SG, Schwaiger M. In vivo molecular imaging of angiogenesis, targeting alphavbeta3 integrin expression, in a patient after acute myocardial infarction. Eur Heart J 2008;29:2201.
11. Spuentrup E, Botnar RM, Wiethoff AJ, et al. MR imaging of thrombi using EP-2104R, a fibrin-specific contrast agent: initial results in patients. Eur Radiol 2008;18:1995–2005.
12. Stehling MK, Turner R, Mansfield P. Echo-planar imaging: magnetic resonance imaging in a fraction of a second. Science 1991; 254:43–50.
13. Irarrazabal P, Nishimura DG. Fast three dimensional magnetic resonance imaging. Magn Reson Med 1995;33:656–662.
14. Sodickson DK, Manning WJ. Simultaneous acquisition of spatial harmonics (SMASH): fast imaging with radiofrequency coil arrays. Magn Reson Med 1997;38:591–603.
15. Pruessmann KP, Weiger M, Scheidegger MB, Boesiger P. SENSE: sensitivity encoding for fast MRI. Magn Reson Med 1999;42: 952–962.
16. Griswold MA, Jakob PM, Heidemann RM, et al. Generalized autocalibrating partially parallel acquisitions (GRAPPA). Magn Reson Med 2002;47:1202–1210.
17. Tsao J, Boesiger P, Pruessmann KP. k-t BLAST and k-t SENSE: dynamic MRI with high frame rate exploiting spatiotemporal correlations. Magn Reson Med 2003;50:1031–1042.
18. Mistretta CA, Wieben O, Velikina J, et al. Highly constrained backprojection for time-resolved MRI. Magn Reson Med 2006;55: 30–40.
19. Candes EJ, Romberg J, Tao T. Robust uncertainty principles: exact signal reconstruction from highly incomplete frequency information. IEEE Trans Inf Theory 2006;52:489–509.
20. Donoho DL. Compressed sensing. IEEE Trans Inf Theory 2006; 52:1289–1306.
21. Lustig M, Donoho D, Pauly JM. Sparse MRI: the application of compressed sensing for rapid MR imaging. Magn Reson Med 2007;58:1182–1195.
22. Stuber M, Gilson WD, Schar M, et al. Positive contrast visualization of iron oxide-labeled stem cells using inversion-recovery with ON-resonant water suppression (IRON). Magn Reson Med 2007; 58:1072–1077.
23. Mani V, Briley-Saebo KC, Itskovich VV, Samber DD, Fayad ZA. Gradient echo acquisition for superparamagnetic particles with positive contrast (GRASP): sequence characterization in membrane and glass superparamagnetic iron oxide phantoms at 1.5T and 3T. Magn Reson Med 2006;55:126–135.
24. Dahnke H, Liu W, Herzka D, Frank JA, Schaeffter T. Susceptibility gradient mapping (SGM): a new postprocessing method for positive contrast generation applied to superparamagnetic iron

oxide particle (SPIO)-labeled cells. Magn Reson Med 2008;60: 595–603.
25. Andia ME, Saha P, Wiethoff AJ, et al. Uptake of a fibrin-targeted contrast agent could direct therapy following deep vein thrombosis. In: Proceedings of the 18th Annual Meeting of ISMRM, Stockholm, Sweden, 2010.
26. von Bary C, Makowski M, Preissel A, et al. MRI of coronary wall remodeling in a swine model of coronary injury using an elastin-binding contrast agent. Circ Cardiovasc Imaging 2011;4:147–155.
27. Candes EJ, Romberg J. Practical signal recovery from random projectiones. Wavelet applications in signal and image processing XI, Proc. SPIE Conf. 5914. 2005.
28. Becker S, Bobin J, Candes EJ. NESTA: a fast and accurate first-order method for sparse recovery. Siam J Imaging Sci 2011;4:1–39.
29. Overoye-Chan K, Koerner S, Looby RJ, et al. EP-2104R: a fibrin-specific gadolinium-Based MRI contrast agent for detection of thrombus. J Am Chem Soc 2008;130:6025–6039.
30. Gudbjartsson H, Patz S. The Rician distribution of noisy MRI data. Magn Reson Med 1995;34:910–914.
31. Botnar RM, Stuber M, Danias PG, Kissinger KV, Manning WJ. Improved coronary artery definition with T2-weighted, free-breathing, three-dimensional coronary MRA. Circulation 1999; 99:3139–3148.
32. Etienne A, Botnar RM, Van Muiswinkel AM, Boesiger P, Manning WJ, Stuber M. "Soap-Bubble" visualization and quantitative analysis of 3D coronary magnetic resonance angiograms. Magn Reson Med 2002;48:658–666.
33. Liang D, Liu B, Wang J, Ying L. Accelerating SENSE using compressed sensing. Magn Reson Med 2009;62:1574–1584.
34. Otazo R, Kim D, Axel L, Sodickson DK. Combination of compressed sensing and parallel imaging for highly accelerated first-pass cardiac perfusion MRI. Magn Reson Med 2010;64: 767–776.